### Title

Binary pseudo-random array standards for calibration of 3D optical surface profilers used for metrology with aspheric x-ray optics




### ISBN

9781510654303



### Authors

Munechika, Keiko
Chao, Weilun
Dhuey, Scott
et al.



### Publication Date

2022-10-03

### DOI

10.1117/12.2633163

Peer reviewed

# Binary pseudo-random array standards for calibration of 3D optical surface profilers used for metrology with aspheric x-ray optics

Keiko Munechika,[*,a] Weilun Chao,[b] Scott Dhuey,[c] Ian Lacey,[d] Carlos Pina-Hernandez,[a]
Simon Rochester,[e] and Valeriy V. Yashchuk,[d]
[a]HighRI Optics, Inc., 5401 Broadway Terr, St. 304, Oakland, CA 94618, USA;
[b]Center for X-ray Optics, Lawrence Berkeley National Laboratory, Berkeley, CA94720, USA;
[c]Molecular Foundry, Lawrence Berkeley National Laboratory, Berkeley, CA, 94720, USA;
[d]Advanced Light Source, Lawrence Berkeley National Laboratory, Berkeley, CA 94720, USA;
[e]Rochester Scientific, LLC, 2041 Tapscott Avenue, El Cerrito, CA 94530, USA

## ABSTRACT

High-accuracy surface metrology is vitally important in manufacturing ultra-high-quality free-form mirrors designed to manipulate x-ray light with nanometer-scale wavelengths. The current and potential capabilities of x-ray mirror manufacturing are limited by inherent imperfections of the integrated metrology tools. Metrology tools are currently calibrated with super-polished flat test-standard/reference mirrors. This is acceptable for fabrication of slightly curved x-ray optics. However, for even moderately curved aspherical x-ray mirrors the flat-reference calibration is not sufficiently accurate. For micro-stitching interferometry developed for surface measurements with curved x-ray mirrors, the tool aberration errors are known to be transferred into the optical surface topography of x-ray mirrors. Our approach to improving metrology is to thoroughly calibrate the measuring tool and apply the results of the calibration to deconvolution of the measured data. Here we explore the application of a recently developed technique for calibrating the instrument transfer function (ITF) of 3D optical surface profilers to metrology with significantly curved x-ray optics. The technique, based on test standards patterned with two-dimensional (2D) binary pseudo-random arrays (BPRAs), employs the unique properties of the BPRA patterns in the spatial frequency domain. The inherent 2D power spectral density of the pattern has a deterministic white-noise-like character that allows direct determination of the ITF with uniform sensitivity over the entire spatial frequency range and field of view of an instrument. The high efficacy of the technique has been previously demonstrated in application to metrology with flat and slightly curved optics. Here, we concentrate on development of an efficient fabrication process for production of highly randomized (HR) BPRA test standards on flat and 500-mm spherical optical substrates. We also compare and discuss the results of the ITF calibration of an interferometric microscope when using the HR BPRA standards on flat and curved substrates.

**Keywords:** surface metrology, calibration, instrument transfer function, binary pseudo-random, test standard, power spectral density, aspheric optics, x-ray optics.

## 1. INTRODUCTION

Optical manufacturing is a multi-billion-dollar industry that is an indispensable part of modern technology and science. The performance of any optical manufacturing process directly depends on the ability of its integrated optical surface metrology method to provide trustworthy feedback. High-accuracy metrology is vitally important in manufacturing ultra-high-quality free-form mirrors designed to manipulate x-ray light with nanometer-scale wavelengths. Due to the shorter wavelength, requirements for the surface figure and finish of x-ray mirrors are three orders of magnitude more stringent than for visible-light optics. Correspondingly, the metrology integrated into x-ray mirror manufacturing that is mostly based on visible-light optical tools must ensure the accuracy of optical surface fabrication on the sub-nanometer level. Improvements are needed not only for the classical plane, spherical, and sagittal cylindrical x-ray mirrors, but, even more urgently, for free-form aspherical x-ray mirrors with moderately and strongly curved shapes, such as paraboloids, ellipsoids, hyperbolas, diaboloids, etc. (see, for example, Refs. [1-5] and references therein). Availability of such mirrors on the market will directly advance the fundamental and applied research performed at x-ray light facilities [6-10].

*km@highrioptics.com; phone 1 800 470 7902; https://highrioptics.com

The limited accuracy of the available metrology for highly curved aspherical optics specified with nanometer or smaller height tolerances has led to an absence in the market of such x-ray mirrors with the optical surface quality required for modern applications. It is the deficiencies in the metrology, rather than in the fabrication technologies [such as the Elastic Emission Machining (EEM) and Electron Beam Figuring (EBF) techniques], that primarily limits the optical quality. Ironically, it is the high resolution of the fabrication techniques that allows the errors in metrology to be observed, by "printing" the metrology errors onto the fabricated surfaces. Therefore, advanced integrated metrology is key to the improvement of optical manufacturing.

The current capabilities and possibility for improvements in x-ray mirror manufacturing are limited by inherent imperfections of the integrated metrology tools. Developing new higher-accuracy metrology instruments to replace the currently integrated tools would be a slow, expensive, and uncertain process. A much more attractive approach is to improve the existing tools by developing calibration techniques to thoroughly characterize them and then to process the data to remove the effects of their imperfections.

In the area of x-ray optics, long trace profilers (LTP) [11-14] are the state-of-the-art one-dimensional (1D) optical metrology instrumentation, widely used for measuring performance and tuning x-ray mirrors and diffraction gratings [15-21]. It was demonstrated experimentally [22,23] that the raw measured results can be very misleading because of the tool's imperfections. It was also demonstrated that the data can be effectively corrected (reconstructed) [23,24] based on high-accuracy calibration of the profiler's modulation (or, more generally, instrument) transfer function (MTF or ITF) [25]. Nearly diffraction-limited focusing of soft x-rays was achieved when close attention was given to characterization of metrological equipment [24].

The vital necessity for a commonly accepted method for the thorough calibration of metrology tools designed for two-dimensional (2D) topography measurements can be illustrated by the example of scanning and transmission electron microscopy (SEM and TEM). SEM makers have often characterized their tools by "beam size" and "resolution," using their own definitions rather than standard measures of technical performance [26]. Thus, the complex correlation between the tool setup and the quality of the topography images or data was very subjective and could not be used for improvement and reliable comparison of SEM instrumentation. On the contrary, the fast progress in TEM was based on the availability of natural test samples such as gold crystals. This allowed for the measurement of the instrument MTF and in this way facilitated the comprehensive characterization of TEM [27]. This leaves no room for arbitrary methods and definitions, so equipment makers had to compete on the level of the *quantified* performance.

A similar, tool-calibration and successive data-deconvolution approach is the foundation of our work on development of high accuracy metrology for state-of-the-art x-ray mirrors and variable-line-spacing (VLS) x-ray diffraction gratings [28-30]. In this case, we exploit the ITF calibration technique based on binary pseudo-random (BPR) test standards [31-33] (see also Sec. 2, below). We aim to significantly improve the accuracy and extend the application range of the metrology techniques such as the Micro-Stitching Interferometry (MSI) and Relative Angle Determinable Stitching Interferometry (RADSI) developed at Osaka University [34-36] and now in use for x-ray optics fabrication at JTEC Corporation (Japan) for the production of high-precision x-ray mirrors [37].

Here, we report the first results of our efforts to extend the ITF calibration technique based on BPR test standards [31-33] to optical interferometry and interferometric microscopy metrology for strongly curved aspheric x-ray optics. The main objective of the project is to develop 2D surface height topography metrology integrable into free-form x-ray mirror manufacturing.

This paper is structured as follows: After a brief overview of the major problems of metrology integrated to optical fabrication systems, including geometrical distortion and limited resolution (Sec. 2), we review the ITF calibration technique based on BPR test standards and describe the BPR standards now available for the ITF calibration of a broad spectrum of metrology instrumentation (Sec. 3). Section 4 presents the details of fabrication and provides the major geometrical and optical parameters of the developed BPRA test standards, as well as checkerboard samples, fabricated for the calibration of microscope lens (geometrical) distortion. The variable parameters include the elementary (minimum) size of the pattern, surface reflectivity, shape of the substrates, etc. The results of the ITF and lens distortion calibration of an optical interferometric microscope available in the Advanced Light Source (ALS) X-Ray Optics Laboratory (XROL) [38,39] with the developed test standards are discussed in Sec. 5. In conclusion (Sec. 6), we briefly review the current status of our project on development of high accuracy metrology for strongly curved aspheric x-ray optics and outline the directions of future research.

## 2. PROBLEMS OF METROLOGY INTEGRATED WITH OPTICAL FABRICATION

The optical fabrication processes used for manufacturing aspherical x-ray mirrors with moderate surface curvature mainly employ surface metrology techniques based on large-aperture interferometry in combination with micro-stitching interferometric microscopy [34-37,40-45]. The metrology provides three-dimensional surface profile data that is converted to a feedback "removal function" used to correct for surface figure and finish errors in the deterministic polishing process as schematically shown in Fig. 1. The quality and cost of the optics directly depends on the accuracy and speed of the integrated metrology, which contributes up to 40-50% to the cost.

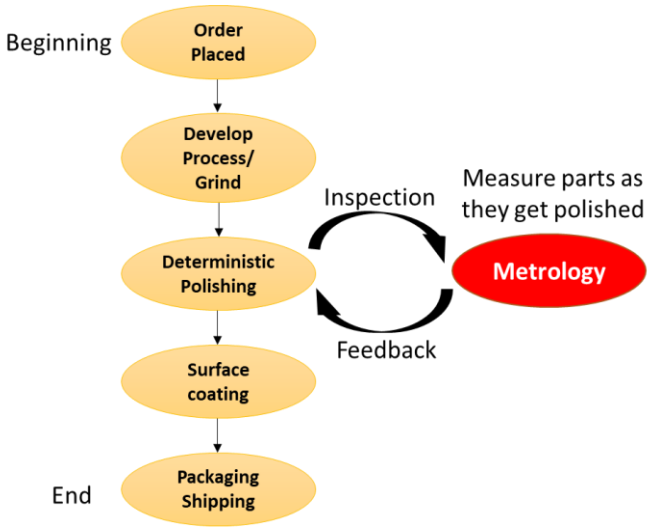


Figure 1: The optical manufacturing process. Polishing is critical and can be the most difficult step depending on the tolerance. The surface is measured as it is polished to provide feedback. "If you can't measure it, you can't make it." (Figure adapted from https://blog.lacroixoptics.com/blog/intro-to-optics-manufacturing).

X-ray mirrors are complex and expensive optical elements with challenging technical requirements. In addition to metrology integrated with the fabrication processes, a variety of ex situ surface metrology techniques are used to verify and, if possible, optimize the beamline performance of the fabricated optics. Their geometry is measured by optical interferometric techniques to assure nearly perfect shape; the surface quality at higher spatial frequencies is characterized by SEM and atomic force microscopy (AFM) to ensure small scattering of x-rays and correct phase properties of the reflected diffraction-limited x-ray beams; additionally, the quality of multilayer and single-layer coatings is studied by TEM and SEM, as well as AFM.

All these tools involved in optical fabrication and beamline performance optimization suffer from random errors, instrumental and set-up instabilities (temporal drifts), and systematic errors. In general, the relatively high-frequency random noise is significantly reduced by averaging multiple repeatable measurements. However, the repeatable measurements with extended data acquisition time can be affected by relatively slow temporal drifts. In some cases, the drift errors can be effectively suppressed by application of a special data acquisition technique based on so-called advanced optimal scanning procedures [46,47]. Unlike both the random and drift errors that are not temporally stable, the systematic errors are characteristic and repeatable for the particular metrology tool and measurement arrangement. Therefore, high precision characterization (calibration) of the systematic errors can be effectively used to improve the accuracy and reliability of the metrology.

In this section, we briefly overview the calibration technique used to characterize the two major systematic errors in topography measuring tools, including surface height metrology with optical interferometers and interferometric microscopes. These are the errors related to the geometrical lateral distortion of the topography in the recorded image and limited spatial resolution of the instrument (see also the relevant discussions in Refs. [30, 48-50]).

### 2.1 Geometrical lateral distortion

Generally, one of the major requirements for imaging systems is to form an image that is geometrically similar to the inherent object topography. However, due to the multiple sources of aberration in imaging systems, the recorded image

often systematically deviates from the ideal geometry of object perspective projection. The deviations from the ideal image geometry (geometrical distortion) can be calibrated with a test artifact with a regular grid of geometric structures like a checkerboard (see Sec. 5) or 1D and 2D lines [51,52]. The geometrical distortion when precisely calibrated can be accounted for in image processing (see, for example, Refs. [18-25] and references therein).

In Sec. 5, we consider the effects of geometrical distortion in interferometric microscope measurements with flat and curved surfaces under test (SUTs). Although geometrical distortion has a negligible effect on the surface roughness measurements, it can cause a significant misrepresentation of the SUT topography in both height and special frequency domains, leading to significant errors in measurements of topographical objects like diffraction gratings (see, for example, Ref. [30] and references therein). In surface metrology with stitching [34-36], unaccounted-for geometrical distortions lead to topographical errors. While the errors can be acceptable for slightly curved x-ray optics, they appear to be significant in the case of even moderately curved aspherical x-ray mirrors. Thus, the aberration errors of the micro-stitching metrology used in the EEM deterministic nano-fabrication process [40,43,45] that depends on the surface curvature, are often transferred into the optical surface topography of x-ray mirrors where they result in quasi-periodic errors in the surface height and slope [53].

### 2.2 Limited lateral resolution and ITF calibration

Even when topography images appear to be of very high visual quality, instrument resolution may be a limiting factor in manufacturing quality. For example, in the case of the quasi-periodic error in the surface height and slope topographies of aspherical x-ray mirrors discussed in Ref. [53], the limited resolution of the slope profiler used for the measurements has led to underestimation of the error amplitude by a factor of more than two. This has become evident only after a precision ITF calibration of the profiler [22] and application of the calibration to reconstruct (deconvolve) [24] the measured data.

The ITF is used for comprehensive quantitative characterization of the spatial resolution (spatial frequency response) of a metrological instrument [25,54-58]. To the extent that the response of the instrument can be characterized as a linear system, the measured PSD, $PSD_{MES}$, is a product of the inherent PSD for the SUT, $PSD_{SUT}$, and the MTFs of the individual components (objective, detector, etc.) of the instrument:

$$PSD_{MES} = PSD_{SUT} \times ITF^2 . \quad (1)$$

The ITF in Eq. (1) is the total MTF of the instrument. It can be experimentally determined by comparing the measured PSD distribution of a test artifact to the corresponding ideal PSD distribution, which is numerically simulated or found from PSD measurements with an instrument with significantly higher resolution. The square root of the ratio of the measured PSD distribution to the ideal PSD distribution gives the MTF of the instrument.

However, ITF characterization, especially in application to 2D metrology, is not widely used because the implementation is complex and dedicated test samples with the required spatial frequencies are not available. This is in spite of the fact that a number of methods for ITF measurement have been developed [59-72]. The effectiveness of a given method hinges critically on the appropriate choice of test surface. A successful test surface should be suitable for calibration over the entire instrumental field of view with a uniform sensitivity to the ITF over the entire spatial frequency range up to the Nyquist frequency of the instrument. Additionally, in order to be used as a certified standard, the ITF test surface should satisfy the conditions of ease of specification, reproducibility, and repeatability; and the accuracy of the ITF calibration should have a reasonably low sensitivity to possible fabrication imperfections of the surface. Most of the common test patterns used in ITF measurements, including knife-edge sources (step height standards) [59–63], bar targets [64], sinusoidal surfaces [65], periodic and quasiperiodic patterns [66-69], white noise patterns [70], and random reference specimens [67,70-72] fail to meet all these requirements. For a comprehensive review of standard reference specimens, especially those used for calibration of optical interferometers and interferometric microscopes, see Refs. [57,58,73-75] and references therein.

In addition to the absence of test standards for comprehensive calibration of the ITF of metrology tools, there are no suitable data processing algorithms and software that can automatically accomplish the ITF calibration and implement it for correction (reconstruction) of the metrology data in the metrology, rather than subjective, ‘by eye’, fashion. The global goal of our research project under development is to provide a turnkey solution for this complex problem.

## 3. ITF CALIBRATION TECHNIQUE BASED ON BPR TEST STANDARDS

In this work, we continue to explore the ITF calibration techniques based on test standards structured according to binary pseudo-random 1D sequences (BPR gratings, BPRGs) and 2D arrays (BPRAs) originally proposed in 2007 [31-33]. The term 'pseudo-random' means that the pattern is deterministic but has the spatial and spectral characteristics of random noise. Depending on the application, the suitable test artifact is patterned as a random distribution of two ('binary') physical properties (e.g., two surface heights, or two materials with different reflectivity, transmission, absorption, work function of an electron, etc.) – Fig. 2.

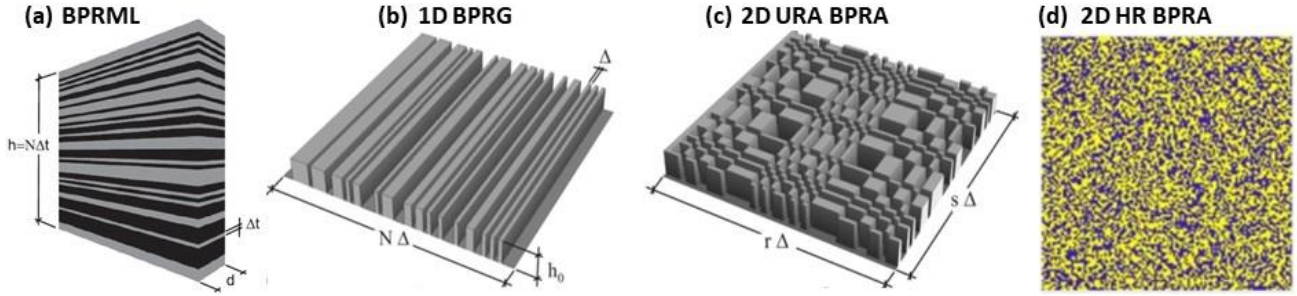


Figure 2: (a) Binary pseudo-random multi-layer (BPRML), (b) 1D BPR grating (BPRG), both designed using maximum-length pseudo-random sequences, (c) and (d) the 2D BPR array patterns designed using uniformly redundant (URA BPRA) and the highly randomized (HR BPRA) arrays.

In this respect, the technique is applicable to practically any topography-measuring instrument. Indeed, a broad variety of BPR test standards with the elementary sizes from 1.5 nanometers and up to the dozens of microns (Fig. 3) have been developed and successfully applied for resolution calibration of the electron, x-ray, and optical microscopes, optical scatterometers, and large-aperture Fizeau interferometers (see, for example, Refs. [76-84] and references therein).

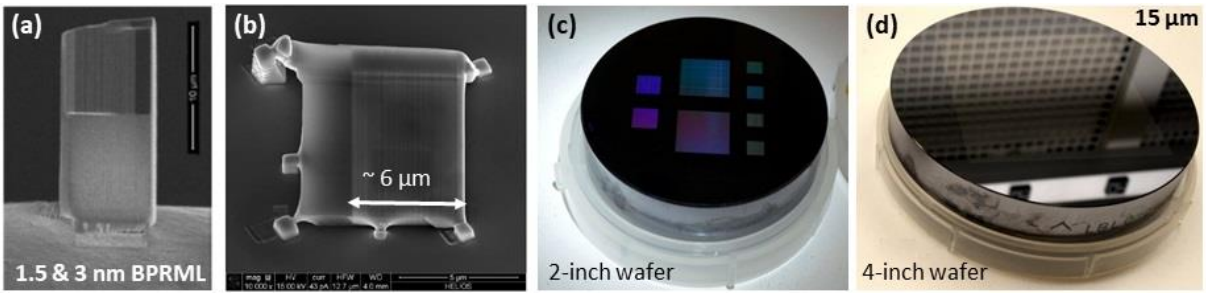


Figure 3: The binary pseudo-random test standards: (a) BPR multilayer (BPRML) samples for the ITF calibration of TEMs and x-ray microscopes; (b) BPRML for the ITF calibration of SEMs and AFMs; (c) multiple 1D BPRG and 2D BPRA patterns with different smallest feature (elementary) sizes from 400 nm to 2 µm etched to a 2-in diameter super-polished silicon substrate are designed for calibration of optical microscopes and scatterometers; BPRA pattern with elementary size of 15 µm etched to a 4-in diameter super-polished silicon substrate is designed for the ITF calibration of large aperture Fizeau interferometers.

The 1D BPR structures (BPRGs and BPRMLs) in Figs. 2 and 3 are built as maximum-length pseudo-random sequences with perfectly constant inherent PSD evaluated over the entire sequence [85-87]. For the ITF calibration of 2D surface topography imaging systems, we have developed binary pseudo-random array standards patterned with uniformly redundant [88,89] and highly randomized [83] binary arrays, URA BPRAs and HR BPRAs (Figs. 2 and 3). Similar to the maximum-length pseudo-random sequences, the URA patterns have inherent PSD distributions that are perfectly constant when evaluated over the entire array. Because of a relatively well-ordered layout of the URA-based BPRAs, these standards, besides their use for ITF calibration, can be used for characterization of the microscope geometrical distortion [30].

A distinguishing property of the BPR standards is their inherent power spectral density (PSD) that has a deterministic white-noise-like character. This allows direct determination of the ITF with uniform sensitivity over the entire spatial frequency range and field of view of the instrument under test. As such, the BPR standards satisfy the characteristics of a

certifiable ITF calibration artifact: functionality, ease of specification and fabrication, reproducibility, and low sensitivity to manufacturing errors.

# 4. FABRICATION OF THE BPR TEST STANDARDS

In this section, we briefly summarize the fabrication and the main parameters of the BPR test standards developed so far for the ITF calibration of the broad spectrum of topography measuring instrumentation.

## 4.1 BPRML samples for the IFT calibration nano-resolution microscopes

The minimum feature size of the pseudo random test sample determines the inherently flat portion of the sample's PSD. For nanometrology systems, the minimum feature size should be as small as possible. BPR test sample requirements are:

- The best possible resolution, under 2 nm minimum feature size
- Materials should provide good contrast in imaging tools (including electron microscopes)
- Materials should be conductive to avoid charging
- Size: a few micrometers (larger than the field of view)
- Line edge roughness significantly less than line width
- Reproducible fabrication technology

Test samples meeting these requirements cannot be fabricated using modern electron-beam lithography techniques. To circumvent limitations found with other fabrication techniques, the pseudo-random structure was produced by depositing a multilayer of two alternating materials using magnetron sputter deposition and then sectioning the stack [80]. The sectioned side of the multilayer is used for subsequent metrology instrumentation characterization. In addition to high electrical conductivity, the material and deposition process requirements are:

- Low surface and interfacial mixing roughness
- Significant difference in mass density
- Low stress

The multilayer material system utilized for the sample, silicon and tungsten silicide, have been used extensively for fabrication of other types of thick multilayer structures [90], and the 1.5 nm smallest layer thickness is still significantly larger than the minimum requirement for good layer contrast. A custom magnetron sputtering system with multiple targets [91] was used for deposition. The targets were 75 mm diameter by 6.25 mm thick disks. The tungsten silicide target was hot-pressed, and the silicon target was boron-doped to facilitate DC sputtering. The system was controlled by a computer with the thicknesses of the deposited layers corresponding to the designed values of pseudo-random pattern. 4095 unit layers were deposited to form the multilayer coating with the designed pseudo-randomly distributed thicknesses on a thick, polished silicon wafer. After that, a focused ion beam (FIB) of a dual beam FEI system was used to remove a vertical slice off the top of the wafer. The slice was platinum-welded by the FIB to a piece of silicon wafer. A SEM image of the welded test sample is shown in Figure 3b. The sample is comprised of alternating lines, each according to its designed linewidth. A part of the silicon wafer is also seen on the left. The selected materials exhibited good contrast in the image set. The total size of the test sample was approximately 8 μm by 6 μm. The lamellae of the test samples were imaged using TEM.

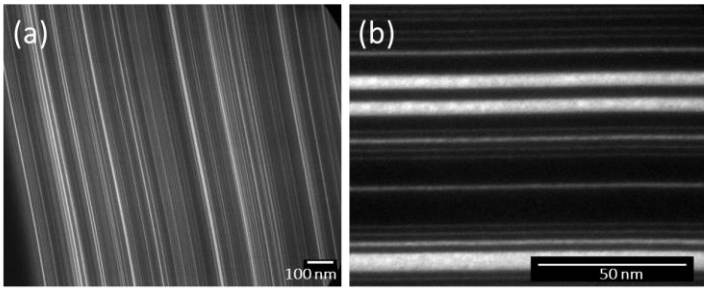


Figure 4: TEM images of the lamella at two magnifications. The mark on the image (a) is 100 nm, the mark on (b) is 50 nm.

### 4.2 BPRA standards for the ITF calibration of large aperture Fizeau interferometers

The field-of-view of the Fizeau interferometer at the XROL has a diameter of 6 inches. At the maximum magnification of around four, the effective pixel size limiting the lateral resolution is about 40 µm. The design of the LBNL sample is based on a BPR array [88, 89] consisting of 4127 × 4129 square elements [78] with the fundamental element dimension of 15 µm so that the squared instrumental MTF can be characterized over the entire dynamic range of the interferometer. Such a sample satisfies the major requirements for a suitable MTF test sample. The lateral size of the smallest feature (the BPRA fundamental size) is smaller by a factor of three than the interferometer lateral resolution at the largest magnification. The height of the BPRA structure is much smaller than the wavelength of the interferometer light of 633 nm.

The BPRA structure was patterned in a chromium layer on the surface of a super polished crystalline silicon substrate with 100 mm diameter and 19 mm thickness using photolithography and a lift-off process. The back side of the substrate was also optically polished and coated with a layer of chromium to decrease the likelihood of deforming the substrate due to the surface tension of the BPRA structure. The total area of the sample is 63.39 x 63.39 $mm^2$, and the step height is about 60 nm. The step height can be tuned by the metal layer thickness. Both the coded-aperture BPRA [82] and the highly randomized (HR) BPRA patterns can be fabricated as shown in Figure 5b and 5c.

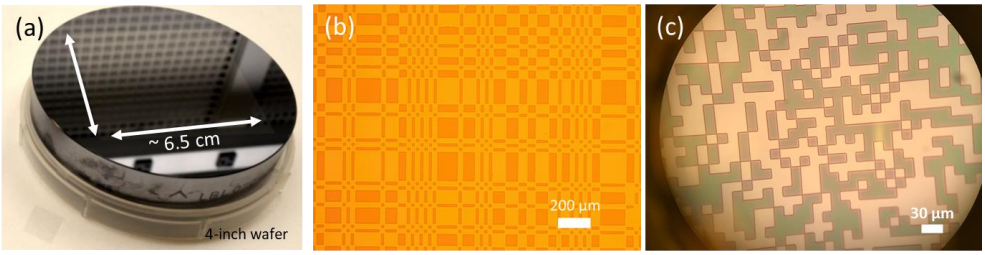


Figure 5: Photograph of the fabricated BPRA test standards with the fundamental size of 15 µm. Optical micrographs of BPRA test standards with different designs: (b) coded aperture and (c) highly randomized (HR) design.

### 4.3 Universal URA and HR BPRA standards for the ITF calibration of optical interferometric microscopes

A test sample which consists of a few different BPRA standards is useful to inspect ITF using a range of imaging arrangements. A "universal" BPRA test standard with elemental size between 400 nm to 2500 nm was designed and fabricated onto a super flat crystalline 2-inch diameter substrate. Both the uniformly redundant array (URA) and highly randomized (HR) BPRA are included in the same substrate, Figure 6a & 6b. The photograph of the BPRA test standard is shown in Figure 6c. There are total of eight BPRA patterns and an additional "step-edge" pattern as summarized in the Fig 6d table. The fabrication was done using electron beam lithography followed by etching. The etch depth of the BPRA is approximately 30 nm. By varying the etch conditions, the etch depth can be easily tuned. The reliability of the BPRA test standards on the etch depth has been studied and reported in Ref. [47].

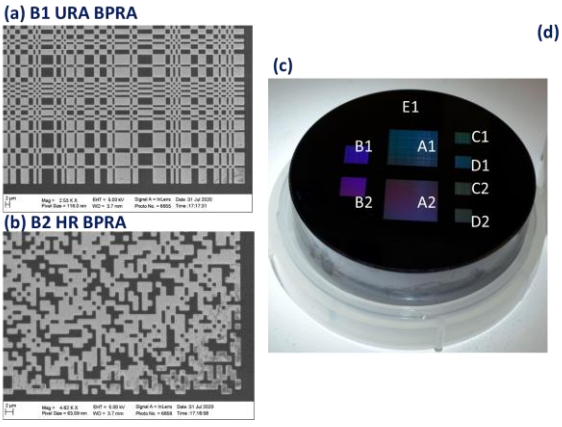


(d)

| Uniformly Redundant Array BPRAs | |
|---|---|
| | Elementary Size [nm] |
| A1 | 2,500 |
| B1 | 1200 |
| C1 | 800 |
| D1 | 400 |
| **Highly Random (HR) BPR Arrays** | |
| A2 | 2,501 |
| B2 | 1201 |
| C2 | 801 |
| D2 | 401 |
| **Single Step** | |
| | Size [mm] |
| E1 | 7.0×7.0 |

Figure 6: "Universal" BPRA standard: (a) Scanning electron micrograph of a section of URA BPRA, (b) scanning electron micrograph of a section of HR BPRA, (c) photograph of the "Universal" BPRA test standard, (d) geometrical parameters of the BPRA patterns.

### 4.4 High resolution HR BPRA standards for the ITF calibration of sub-resolution optical microscopes

To increase BPRA application range to even higher spatial frequencies, high-resolution BPRA standards were developed consisting of BPRA patters with the elementary sizes of 80 nm, 160 nm, and 240 nm. Fabrication was done using electron beam lithography followed by etching using a 1-inch diameter super-polished silicon substrate. Figure 7a shows a photograph of the high-resolution BPRA patterns with 80 nm, 160 nm, and 240 nm elementary sizes. Figure 7b shows a scanning electron micrograph of the section of the BPRA with 80 nm elementary size. Figure 7c table shows the geometrical parameters of the high resolution BPRA. Similar to the "universal" BPRA described in Section 4.4, the etch depth of the BPRA patterns are tested between 15 nm ~ 30 nm deep, controlled by duration of the etch time.

(a)

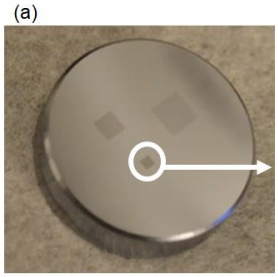

(b)

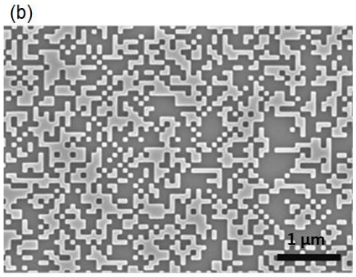


(c)

| High Resolution BPRA | | |
|---|---|---|
| **Pattern Number** | **Elementary Size [nm]** | **BPR Pattern Area, X×Y [mm]** |
| **HR-80** | 80 | 1.369 x 1.369 |
| **HR-160** | 160 | 2.722 x 2.722 |
| **HR-240** | 240 | 4.074 x 4.074 |

Figure 7: (a) photograph of the high-resolution BPRA patterns with 80 nm, 160 nm, and 240 nm elementary sizes fabricated on 1-in diameter Si substrate, (b) a scanning electron micrograph of the section of the BPRA with 80 nm elementary size, (c) geometrical parameters of the high resolution BPRA.

### 4.5 Checkerboard test artifacts for geometrical distortion calibration of optical microscopes

As a proof of concept, we have tested patterning onto a slightly curved, concaved lens with a radius of curvature (ROC) of 500 mm. We used a BPRA pattern with elementary size of 400 nm as well as checkerboard patterns with smallest feature size of 1.5 µm and 3.0 µm. The overall size of the BPRA pattern is 3.39×3.39 $mm^2$, while the checkerboard patterns are 3.0 x 3.0 $mm^2$ and 3.6 × 3.6 $mm^2$ for the 1.5 µm and 3.0 µm elementary sizes, respectively. Performing nanolithography onto a non-flat surface is challenging and possibly introduces errors such as non-uniform thickness in the resist. Since the curvature was not too severe, we performed the initial tests with electron beam lithography to pattern onto the concave surface. The height (h) between the highest point and the lowest point of the pattern area is approximately 2.25 µm, which was still sufficiently low enough to be compensated by the e-beam writer. The concaved side of the lens was first coated with a thin layer of Cr. Once the lithography was performed and developed, another thin layer (~ 40 nm) of Cr was deposited for lift-off process. Figure 8a shows the photograph of the actual checkerboard pattern on a concaved lens. Figure 8b shows the checkerboard design.

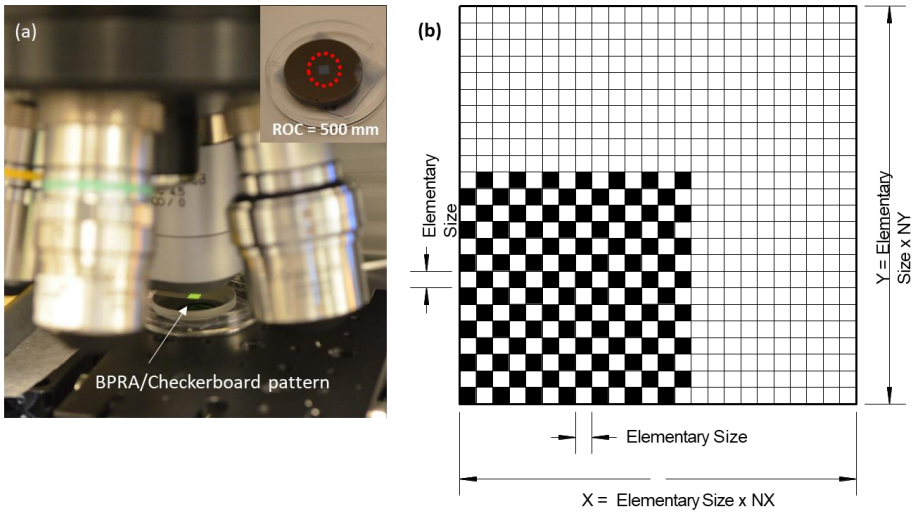


Figure 8: (a) photograph of the BPRA / Checkerboard pattern under inspection. The inset photograph shows the fabricated checkerboard pattern onto a concaved substrate with the ROC of 500 mm. (b) A section of the checkerboard design file.

### 4.6 Major geometrical and optical parameters of the developed BPRA standards

The fundamental elemental size and the overall pattern area of the BPRA standards are selected so that the geometrical parameters of the BPRA are suitable for characterizing the ITF of the tool for a given measurement arrangement. Table 1 summarizes the currently available BPRA geometrical parameters, primarily designed for optical microscopes and Fizeau interferometers. The elemental size of the BPRA should be smaller than the pixel size of the measuring instrument. For example, the ZYGO NewView-9000 with 50× objective and 1.0× zoom has a pixel size of 0.172 μm, according to the manufacturer's specification, therefore, the most suitable BPRA is HR-80, which will cover the spatial frequency range between 80 nm and 1.369 mm. For ultra-high resolution 1D multi-layers, Table 2 lists available BPR lamellas.

Table 1. The list of available BPRA test standards. Each pattern represents BPRA test standards with varying minimum feature sizes.

| **Available Binary Pseudo Random Arrays** | | |
|---|---|---|
| **Pattern Number** | **Elementary Size [nm]** | **BPR Pattern Area, X×Y [mm]** |
| **HR-80** | 80 | 1.369 × 1.369 |
| **HR-160** | 160 | 2.722 × 2.722 |
| **HR-240** | 240 | 4.074 × 4.074 |
| **HR-400** | 400 | 3.39×3.39 |
| **HR-800** | 800 | 3.39×3.39 |
| **HR-1200** | 1200 | 5.08×5.08 |
| **HR-2500** | 2500 | 10.57×10.57 |
| **HR-15000** | 15000 | 63.39 × 63.39 |

Table 2. The list of available BPR lamellas. The smallest elementary size is 1.5 nm. BPR lamellas are cut into slices and mounted onto a substrate.

| **BPR Ultra High Resolution (1D) multi-layers** | | |
|---|---|---|
| Product Number | Elementary Size [nm] | Total Size |
| **Lamella1.5** | 1.5 | BPR width = 6 μm, BPR is sliced to order |
| **Lamella3.0** | 3 | BPR width = 6 μm, BPR is sliced to order |

## 5. CALIBRATION OF THE ALS XROL INTERFEROMETRIC MICROSCOPE FOR MEASUREMENT WITH CURVED OPTICS

The BPRA standards and test samples described in Secs. 3 and 4 have been used for resolution (ITF) characterization of a broad spectrum of topography measuring system, from x-ray and electron microscopes [77-81], to optical scatterometers [54], interferometers [78,82,83], and microscopes [28,30-33,48-50, 84].

The effectiveness of ITF calibration using the BPR technique has been investigated and confirmed in multiple measurements with different metrology tools. For interferometric microscopes, it was shown [49,50,84] that the results of the ITF calibration are independent of the BPRA pattern depth, surface reflectivity, and the elementary size of the pattern, if it is smaller than the microscope lateral resolution by a factor > 2. In addition, the tests with the BPRA have allowed us to bring to light the strong dependence of the ITF calibration on the microscope optical arrangement (magnification and focusing), data acquisition settings, and environmental conditions (such as vibration).

In this section, we present the first results of investigation of dependence of the ITF and geometrical distortion calibration of an interferometric microscope on the curvature of the SUT.

### 5.1 ITF calibration with HR BPRA standard on a 500-mm spherical substrate

Figure 9 depicts the surface height distribution of the HR BPRA standard with 400 nm elementary size fabricated on a 1-in diameter spherical substrate with 500 mm ROC. The measurement is performed with the ALS XROL interferometric microscope equipped with the 20× objective at 1× zoom. In this case, the BPRA elementary size of 400 nm is significantly smaller than the microscope's resolution limit of ~ 690 nm (the Abbe diffraction limit at the objective NA=0.40). In such case, the microscope lateral resolution is mostly limited by the microscope optical system, rather than the effective pixel size.

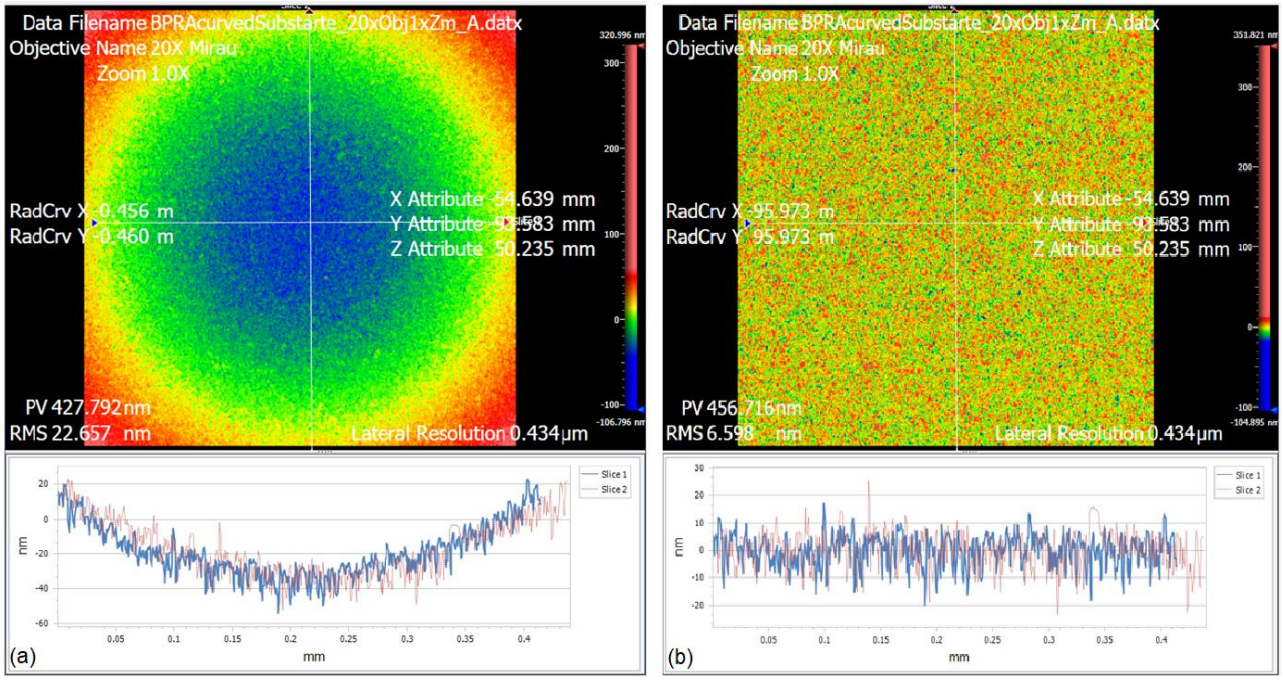


Figure 9. Surface height distribution of the HR BPRA standard with 400 nm elementary size fabricated on a 500-mm spherical substrate as measured with the ALS XROL interferometric microscope equipped with 20× at 1× zoom: (a) the raw data with a reference surface subtracted; (b) the same data as in plot (a) but additionally detrended with the best-fit spherical surface with ROC of approximately 460 mm.

The data preprocessing is performed with the native instrument software. First, a reference surface, specially measured over a super-polished flat reference substrate at the same microscope arrangement, is subtracted (Fig. 9a). Then, the overall shape variation is detrended with the best-fit spherical surface with radius of curvature of approximately 460 mm (Fig. 9b).

Next, the detrended data are processed with custom software developed for PSD processing, ITF model parametrization, and ITF-based deconvolution of measured data [28-30]. Figure 10 presents the software screenshot corresponding to the comparison of two measurements, the first over the 1-in dia. HR BPRA pattern on the spherical substrate (Fig. 9b) and the second over a similar 400-nm HR BPRA fabricated on a flat substrate measured at the same microscope arrangement, 20× objective at 1× zoom.

In Fig. 10, the data corresponding to the BPRA on spherical substrate are loaded to the software as 'Measured' data (the top-left 2D image in the screenshot in Fig. 10). The root-mean-square (rms) variation of this height data is about 6.5 nm. The data corresponding to the 400-nm BPRA on the flat substrate are the 'Reference' data (the top-right image). The rms variation of the 'Reference' data measured is about 2.1 nm that is significantly smaller than that of the BPRA pattern on the spherical substrate. The difference is due to the etched depth of the patterns that differ by a factor of ~ 3.

The corresponding 1D PSD distributions in the vertical and horizontal directions are shown in the bottom right plots of the screenshot (Fig. 10) with the blue and green curves for the 'Measured' and 'Reference' data, respectively.

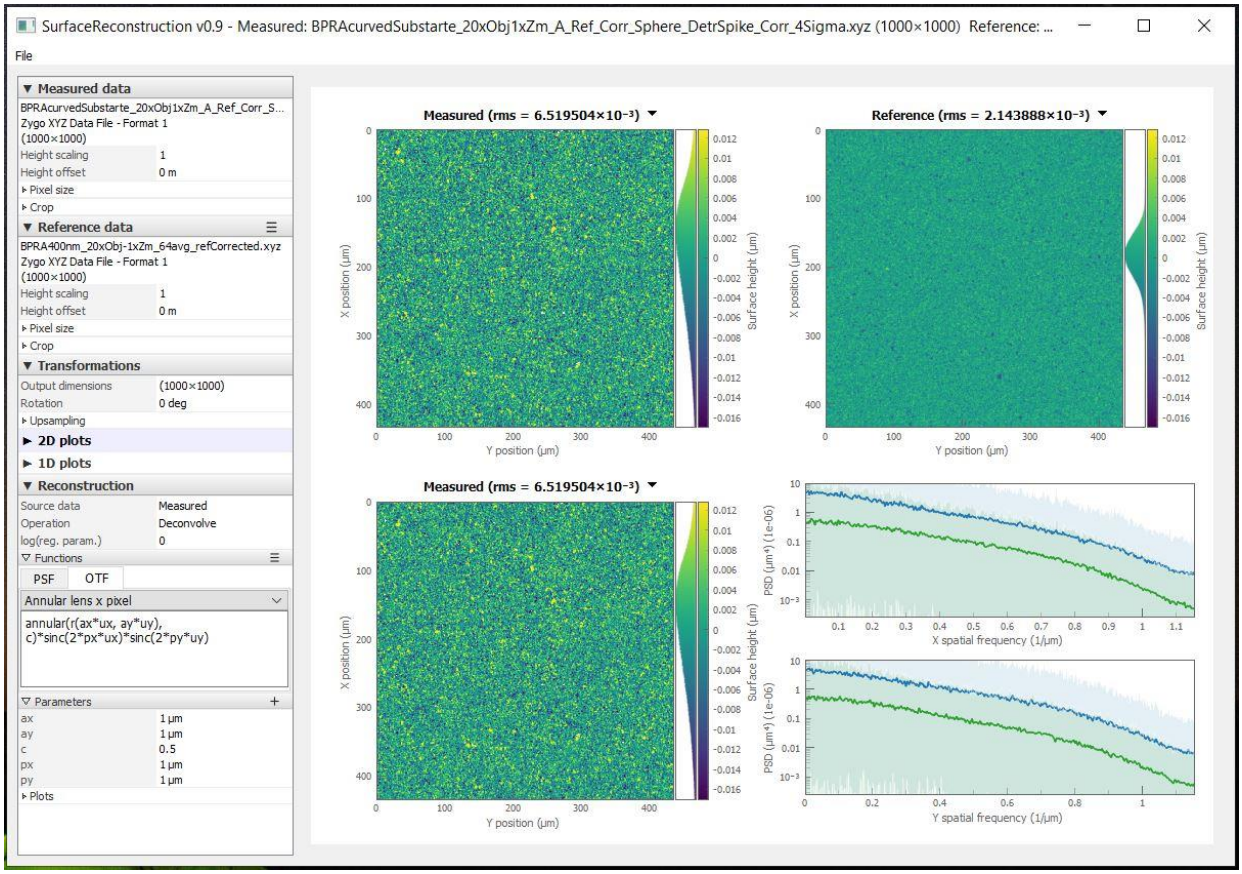


Figure 10. (a) A screenshot of the original software developed for the ITF calibration of metrology profilometers and ITF-based deconvolution of the measured data [28-30]. The data shown has been obtained with the interferometric microscope equipped with the 20× objective at 1× zoom.

To understand the dependence of the microscope ITF calibration on the shape of the SUT (in our case, on the shape of the BPRA standard), the 'Reference' data in Fig. 10 are scaled to match the rms variation of the 'Measured' data. The result of the comparison is illustrated in Fig. 11 that presents the corresponding 1D PSD distributions before (a) and after (b) correction of the rms variation.

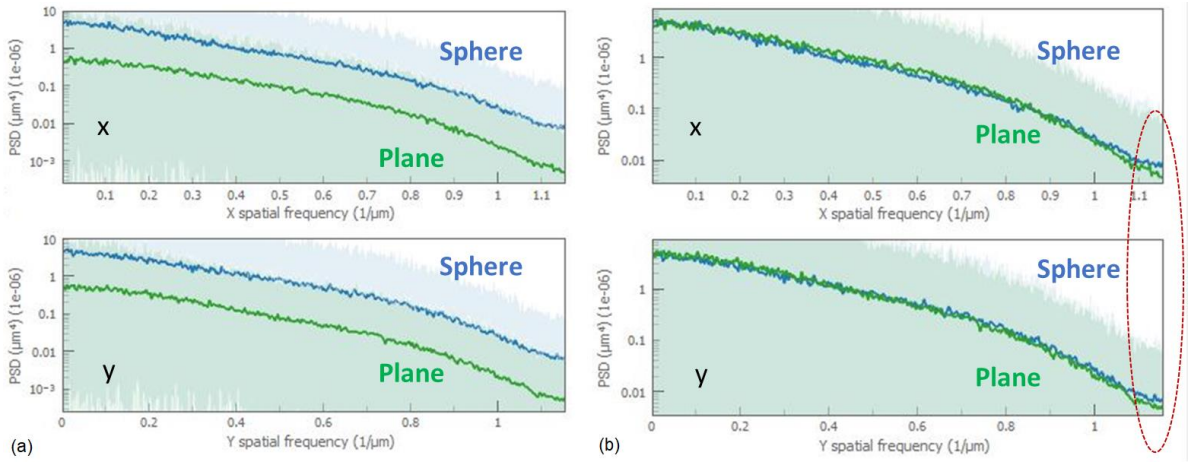


Figure 11: 1D PSD distributions measured with the 400-nm HR BPRA patterns on spherical (blue) and flat (green) substrates, before (a) and after (b) correction to match the rms variations. The dashed red ellipse marks the higher spatial frequency region with the observable difference of the corresponding microscope ITF calibrations.

The small but observable difference of the PSD distributions in Fig. 11b at the higher spatial frequency may be a signature of the difference of the microscope resolution in measurements with the spherical and plane substrates. To provide more conclusive information about the dependence of the microscope ITF on the curvature of surface, we are working on development of an HR BPRA test standard on a significantly more curved substrate.

The data in Figs. 10 and 11 confirms that the fabrication process using electron beam lithography, originally developed to pattern BPRA test standards on flat substrates, is also functional for fabrication of the standards on slightly curved substrates with ROC of ~ 500 mm. However, application of the same fabrication process to significantly more curved substrates is not trivial, especially for the BPRA test patterns where high accuracy in the pattern dimension and placement are critical.

### 5.2 Geometrical distortion calibration with checkerboard sample on flat substrate and on 500-mm spherical substrate

For geometrical distortion calibration, we use the checkerboard test artifact fabricated on a 500-mm ROC 1-in diameter super-polished silicon substrate (Sec. 4.5) – Fig. 12. The checkerboard pattern with elementary size 3.0 μm is etched to the depth of about 45 nm.

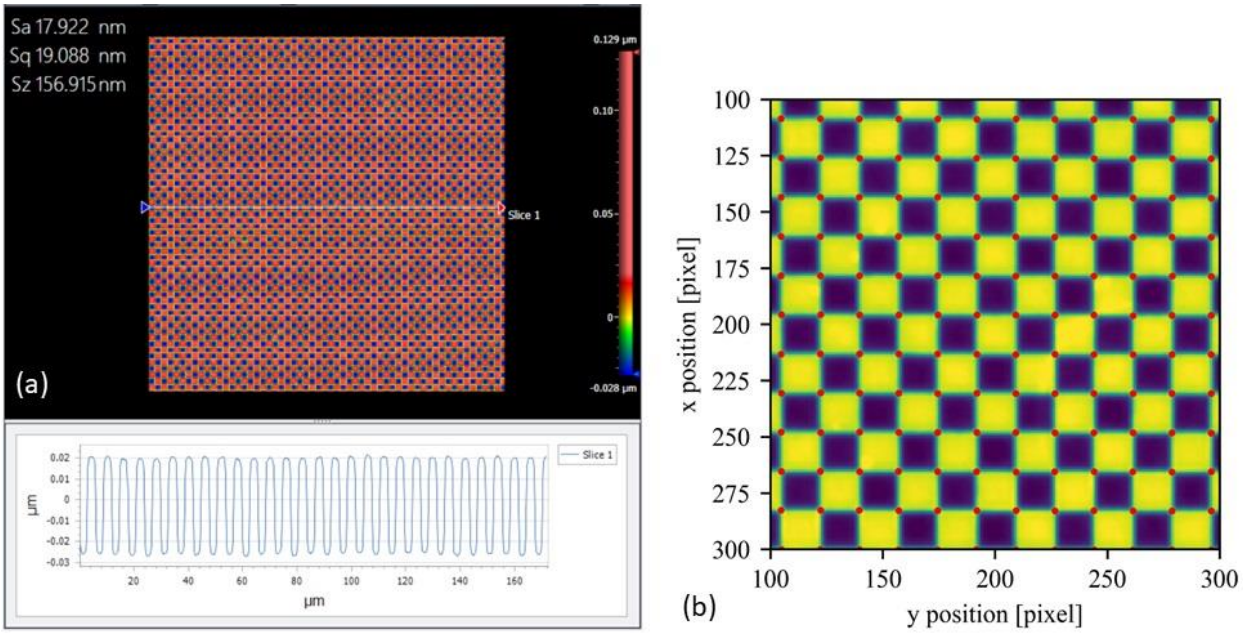


Figure 12. (a) The checkerboard pattern with the elementary sizes of 3.0 μm as measured with the ALS XROL interferometric microscope equipped with 50× objective at 1× zoom. The etched depth of the pattern is about 45 nm as seen on the corresponding sections along the slice line depicted in the image. (b) A 200 x 200-pixel section of a 1000 x 1000-pixel image of the checkerboard; red dots indicate corners found by the algorithm [93] described also in Ref. [30].

For the geometric distortion calibration, the data processing consists in locating and matching characteristic features of the measured and designed (ideal) test patterns (Fig. 12b). The positions of the corners of the checkerboard elements can be found using the existing implementations of sophisticated algorithms, available, for example, in the Open-Source Computer Vision (OpenCV) library [92], for locating the checkerboard corners with high accuracy. Here, for finding the corners (Fig. 12b), we use a method described in Ref. [93] and implemented in OpenCV, which is based on a localized Radon transform implemented by box filters and provides high subpixel accuracy.

The checkerboard image processing is performed in Python using camera calibration routines from the OpenCV library (see also the relevant discussion in Ref. [30]). First, the found corners of the recorded checkerboard image (Fig. 12b) are identified with the projection of the corners of an ideal checkerboard sample from 3D space onto the camera image plane using the pinhole camera model (see, for example, Ref. [94]). Next, the position, rotation, tilt, and magnification of the ideal sample (extrinsic parameters) are varied and the best fit to the measured corners is found.

Similar to Ref. [30], the fitting model includes lens distortion in the form of the lowest-order radial distortion term with the distortion coefficient $k_1$. The distortion procedure shifts each point $(x, y)$ in the image plane by an amount depending on its displacement $(d_x = x - c_x, d_y = x - c_y)$ from a principal (aka the central) point $(c_x, c_y)$, so that

$$x' = d_x(1 + k_1 r^2) + c_x, \tag{2a}$$

$$y' = d_y(1 + k_1 r^2) + c_y, \tag{2b}$$

where $r^2 = d_x^2 + d_y^2$.

Figure 13 shows the residual distances between the measured checkerboard corners from the image (Fig. 12a) and the best-fit projection of the ideal checkerboard corners. When the distortion effect is omitted from the projection model (Fig. 13a), the displacement exhibits $r^3$ dependence with residual distance of up to two pixels at the image corners. Accounting in the projection model for the lowest-order radial camera distortion, given by Eq. (2), the measured and ideal checkerboard patterns match well (Fig. 13b).

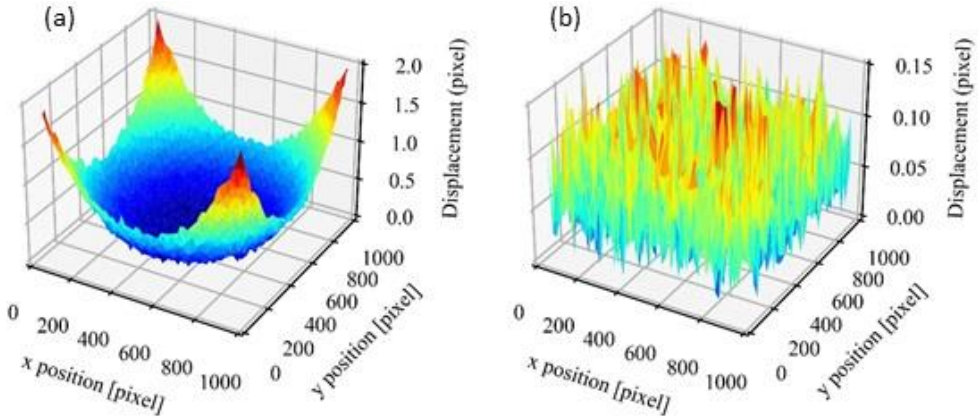


Figure 13. Displacement (in pixels) between the checkerboard corners found from the image and those of an ideal checkerboard projected onto the image, rotating and translating for the best fit. (a) Projection neglects camera distortion; (b) projection accounts for lowest-order radial camera distortion. Note the change in vertical scale.

Similar to the lens distortion observed with flat checkerboard sample, the data obtained with the checkerboard on the 500-mm ROC substrate is well described by the lowest-order term described above [Eq. (2)]. However, the residual distance between projected and measured corners is almost twice higher, about 0.08 of a pixel. This may relate to the higher elementary size of the checkerboards of 3.0 μm compared to 1.5 μm used in Ref. [30].

For the data in Fig. 13, the best-fit distortion parameter is $6.704(88)\times10^{-9}$ pixel$^{-2}$ and the principal point is [490(5) px, 513(2) px]. These parameter values are in good agreement with that of Ref. [30] $6.819(7)\times10^{-9}$ pixel$^{-2}$ and (473 px, 515 px), obtained from the lens distortion calibration with the flat checkerboard sample.

Using the checkerboard square size of 3.0 μm as a reference, we can extract from the performed fitting the corrected microscope's pixel size that is 0.17287(2) μm that is also coincides with the values 0.17289(1) μm found in Ref. [30].

The values of the standard deviations derived here and given in brackets are estimated from the variation of the results of the lens distortion calibration obtained from the measurements over different areas of the checkerboard sample. The comparison of the multiple measurements has allowed us to confirm that the observed distortion (Fig. 13a) is due to the microscope and is not intrinsic to the sample.

The extracted geometrical distortion calibration parameters can be used to reconstruct the surface topography of a measured sample by applying the inverse coordinate transformation and resampling using bilinear interpolation. The results of this procedure applied to measurements of a uniform grating are discussed in Ref. [30].

## 6. DISCUSSION AND CONCLUSIONS

Metrology tools, such as state-of-the-art interferometric microscopes that provide 2D topography data, have limitations in the fine detail they can accurately record, and additionally suffer from geometrical distortion of the image data due to imperfections in the optical systems. We have developed methods to characterize and compensate for limited resolution and geometrical distortion, and in this work, we applied these methods to samples on curved substrates.

To recover surface information at the limit of the instrument's resolution, we use binary pseudo-random test artifacts, BPRAs to measure and deconvolve the instrument transfer function. We have shown that using BPRA patterns with elementary size below the diffraction limit of the tool is effective and yields an unambiguous, generally smooth (low noise), roll-off of the PSD curve. Furthermore, for the case of slightly curved optics, we have shown that the HR-BPRA pattern, on a curved substrate, provides results consistent with flat optics. However, we have found a small, noticeable difference between the PSDs at higher spatial frequencies measured with the same BPRA patterns on the flat and 500-mm spherical substrates. This may be a signature of the difference of the microscope resolution between measurements with the spherical and plane SUTs. To provide more conclusive information about the dependence of the microscope ITF on the curvature of surface, we are working on development of a HR BPRA test standard on a significantly more curved substrate.

Using a checkerboard test artifact fabricated on the 500-mm ROC spherical substrate, we have experimentally demonstrated significant distortion of the imaged artifact pattern due to microscope lens distortion. The extracted lens distortion parameters agree with those obtained in Ref. [30] using a flat checkerboard artifact.

In conclusion, the BPRA test standards provide consistent results that can be used to calibrate world-class metrology instrumentation for a range of applications, from flat optics, to curved optics, to accurately determining grating structures, and with the application of geometrical distortion correction, can enable improved stitching capabilities.


## ACKNOWLEDGEMENTS

The authors are grateful to Ulf Griesmann and Peter Takacs for fruitful discussions. This work was partially supported by the U.S. Department of Energy Office of Science, Office of Basic Energy Sciences, and Small Business Technology Transfer (STTR) programs under Award Numbers DE-SC0011352, DE-SC0022373, and DE-SC0022412 to HighRI Optics, Inc. and Rochester Scientific, LLC. It was also supported by the U.S. NASA STTR programs under Contracts #80NSSC20C0505 and #80NSSC22PB039 to HighRI Optics, Inc. Research at the Advanced Light Source and the Molecular Foundry at Lawrence Berkeley National Laboratory are supported by the Office of Science, Office of Basic Energy Sciences, and Material Science Division of the U.S. Department of Energy under Contract No. DE-AC02-05CH11231.

## REFERENCES


[1] V. V. Yashchuk, I. Lacey, G. S. Gevorkyan, W. R. McKinney, B. V. Smith, T. Warwick, "Ex situ metrology and data analysis for optimization of beamline performance of aspherical pre-shaped x-ray mirrors at the Advanced Light Source," Rev. Sci. Instrum. 90(2), 021711/1-13 (2019); doi: 10.1063/1.5057441.

[2] K. A. Goldberg, "Analytic descriptions of parabolic X-ray mirrors," J. Synchrotron Rad. 29, 985-990 (2022); https://doi.org/10.1107/S1600577522004593.

[3] K. A. Goldberg, "Derivation of closed-form ellipsoidal X-ray mirror shapes from Fermat's principle," J. Synchrotron Rad. 29, 991-996 (2022); https://doi.org/10.1107/S1600577522005793.

[4] V. V. Yashchuk, I. Lacey, and M. Sanchez del Rio, "Analytical expressions of the surface shape of 'diaboloid' mirrors," Proc. SPIE 11493, 114930N/1-13 (2020); doi: 10.1117/12.2568332.

[5] V. V. Yashchuk, K. A. Goldberg, I. Lacey, W. R. McKinney, M. Sanchez del Rio, and H. A. Padmore, "Diaboloidal mirrors: Algebraic solution and surface shape approximations," J. Synchrotron Rad. 28(4), 1031-1040 (2021); http://doi.org/10.1107/S1600577521004860.

[6] Samoylova, L., Sinn, H., Siewert, F., Mimura, H., Yamauchi, K., and Tschentscher, T., "Requirements on hard X-ray grazing incidence optics for European XFEL: Analysis and simulation of wavefront transformations," Proc. SPIE 7360, 73600E/1-9 (2009); https://doi.org/10.1117/12.822251.

[7] Cocco, D., "Recent Developments in UV optics for ultra-short, ultra-intense coherent light sources," Photonics 2015, 2(1), 40-49 (2015); https://doi.org/10.3390/photonics2010040.

[8] Idir, M. and Yashchuk, V. V., Co-Chairs, "Optical and X-ray metrology," in: X-ray Optics for BES Light Source Facilities, Report of the Basic Energy Sciences Workshop on X-ray Optics for BES Light Source Facilities, D. Mills and H. Padmore, Co-Chairs, pp. 44-55, U.S. Department of Energy, Office of Science, Potomac, MD (March 27-29, 2013); http://science.energy.gov/~/media/bes/pdf/reports/files/BES_XRay_Optics_rpt.pdf.

[9] M. Sanchez del Rio, K. A. Goldberg, V. V. Yashchuk, I. Lacey, and H. A. Padmore, "Simulations of applications using diaboloid mirroArs," J. Synchrotron Rad. 28(4), 1041-1049 (2021); https://doi.org/10.1107/S160057752100401X.

[10] Y. Ding, C. Segre, A. Khounsary, "Diaboloid mirror for a bending magnet beamline," Proc. SPIE 11837, 118370A (2021); https://doi.org/10.1117/12.2594663.

[11] Takacs, P. Z., "X-ray optics metrology," in: Handbook of Optics, 3rd ed., Vol. V, M. Bass, Ed., Chapter 46, McGraw-Hill, New York (2009).

[12] Takacs, P. Z., Qian, S., and Colbert, J., "Design of a long trace surface profiler," Proc. SPIE 749, 59-64 (1987); https://doi.org/10.1117/12.939842.

[13] Takacs, P. Z., Feng, S. K., Church, E. L., Qian, S., and Liu, W-M., "Long trace profile measurements on cylindrical aspheres," Proc. SPIE 966, 354-64 (1989); https://doi.org/10.1117/12.948082.

[14] Rommeveaux, A., Thomasset, M., and Cocco, D., "The Long Trace Profilers," in [Modern Developments in X-ray and Neutron Optics], A. Erko, M. Idir, T. Krist, A. G. Michette, Eds., Chapter 10, Springer-Verlag, Berlin/Heidelberg (2008).

[15] Kirschman, J. L., Domning, E. E., McKinney, W. R., Morrison, G. Y., Smith, B. V., and Yashchuk, V. V., "Performance of the upgraded LTP-II at the ALS Optical Metrology Laboratory," Proc. SPIE 7077, 70770A/1-12 (2008).

[16] Senba, Y., Kishimoto, H., Ohashi, H., Yumoto, H., Zeschke, T., Siewert, F., Goto, S., and Ishikawa, T., "Upgrade of long trace profiler for characterization of high-precision X-ray mirrors at SPring-8," Nucl. Instr. and Meth. A 616(2-3), 237-240 (2010).

[17] Irick, S. C. and McKinney, W. R., "Measurement of diffraction gratings with a long trace profiler with application for synchrotron beamline gratings," AIP Conf. Proc. 417, 118-121 (1997); https://doi.org/10.1063/1.54581.

[18] F. Siewert, H. Lammert, G. Reichardt, U. Hahn, R. Treusch, R. Reininger, Inspection of a Spherical Triple VLS-Grating for Self-Seeding of FLASH at DESY, AIP Conf. Proc. 879 (2007) 667–670. https://doi.org/10.1063/1.2436150.

[19] Cocco, D., Sostero, G., Zangrando, M., "Technique for measuring the groove density of diffraction gratings using the long trace profiler," Rev. Sci. Instrum. 74 (2003) 3544–3548; https://doi.org/10.1063/1.1584080.

[20] Thomasset, M., Dvorak, J., Brochet, S., Dennetiere, D., and Polack, F., "Grating metrology for X-ray and V-UV synchrotron beamlines at SOLEIL," Rev. Sci. Instrum. 90, 021714 (2019); https://doi.org/10.1063/1.5055284.

[21] Lacey, I. and Yashchuk, V. V., "Characterization of Groove Density Variation of VLS gratings with ALS XROL LTP-II in different operation modes," Proc. SPIE 11492, 114920D/1-16 (2020); doi: 10.1117/12.2568705.
[22] Siewert, F., Zeschke, T., Arnold, T., Paetzold, H., and Yashchuk V. V., "Linear chirped slope profile for spatial calibration in slope measuring deflectometry," Rev. Sci. Instrum. 87(5), 051907/1-8 (2016); doi: 10.1063/1.4950737.
[23] Yashchuk, V. V., Lacey, I., Anderson, K., Dickert, J., Smith, B.V., and Takacs, P. Z., "Multifunctional light beam source for surface slope measuring long trace profilers," Proc. SPIE 11492, 1149205/1-18 (2020); doi: 10.1117/12.2570462.
[24] Yashchuk, V. V., Rochester, S., Lacey, I., and Babin, S., "Super-resolution surface slope metrology of x-ray mirrors," Rev. Sci. Instrum. 91, 075113/1-11 (2020); doi: 10.1063/5.0005556.
[25] Boreman, G. D., [Modulation Transfer Function in Optical and Electro-optical Systems], SPIE Press, Bellingham, Washington (2001).
[26] D. C. Joy, "Some issues in SEM-based metrology," Proc. SPIE 3332, 102-109 (1998); https://doi.org/10.1117/12.308720.
[27] J. P. McCaffrey and J.-M. Baribeay, "A transmission electron microscope (TEM) calibration standard sample for all magnification, camera constant, and image/diffraction pattern rotation calibrations," Microscopy Res. and Tech. 32, 449-454 (1995); https://doi.org/10.1002/jemt.1070320507.
[28] Munechika, K., Cabrini, S., Chao, W., Lacey, I., Pina-Hernandez, C., Rochester, S., and Yashchuk, V. V., "Binary pseudo-random array test standard optimized for characterization of interferometric microscopes," Proc. SPIE 11817, 1181704/1-10 (2021); doi: https://doi.org/10.1117/12.2594995.
[29] Rochester, S., Munechika, K., Lacey, I., Takacs, P. Z., and Yashchuk, V. V., "Super-resolution image reconstruction for surface metrology of x-ray optics," Poster presentation at the 7th International Workshop on X-ray Optics and Metrology, The SRI2022 Satellite Workshop (IWXM 2022) (Berlin, Germany, April 7, 2022).
[30] Rochester, S., English, D., Lacey, I., Munechika, K., and Yashchuk, V. V., "Super-resolution interferometric microscope measurements with x-ray variable-line-spacing diffraction gratings," SPIE Optics and Photonics 2022, Conference OP501: Advances in Metrology for X-Ray and EUV Optics X, Paper No.: 12240-26 (San Diego, August 21-25, 2022); this conference.
[31] Yashchuk, V. V., McKinney, W. R., and Takacs, P. Z., "Test surfaces useful for calibration of surface profilometers," United States Patent No.: 8,616,044.
[32] Yashchuk, V. V., McKinney, W. R., and Takacs, P. Z., "Binary pseudorandom grating as a standard test surface for measurement of modulation transfer function of interferometric microscopes, Proc. SPIE 6704, 670408 (2007); https://doi.org/10.1117/12.732557.
[33] Yashchuk, V. V., McKinney, W. R., and Takacs, P. Z., "Binary pseudorandom grating standard for calibration of surface profilometers," Opt. Eng. 47(7), 073602-1-5 (2008); https://doi.org/10.1117/1.2955798.
[34] Yamauchi, K., Yamamura, K., Mimura, H., Sano, Y., Saito, A., Ueno, K., Endo, K., Souvorov, A., Yabashi, M., Tamasaku, K., Ishikawa, T., and Mori, Y., "Microstitching interferometry for x-ray reflective optics," Rev. Sci. Instrum., 74(5), 2894-2898, (2003); doi: 10.1063/1.1569405.
[35] Mimura, H., Yumoto, H., Matsuyama, S., Yamamura, K., Sano, Y., Ueno, K., Endo, K., Mori, Y., Yabashi, M., Tamasaku, K., Nishino, Y., Ishikawa, T., and Yamauchi, K., "Relative angle determinable stitching interferometry for hard x-ray reflective optics," Rev. Sci. Instrum. 76, 045102 (2005); https://doi.org/10.1063/1.1868472.
[36] Ohashi, H., Tsumura, T., Okada, H., Mimura, H., Masunaga, T., Senba, Y., Goto, S., Yamauchi, K., Ishikawa, T., "Microstitching interferometer and relative angle determinable stitching interferometer for half-meter-long x-ray mirror," Proc. SPIE 6704, 670405/1-8 (2007); doi: 10.1117/12.733476.
[37] JTEC Corporation, "Nano Measurement Technology;" https://www.j-tec.co.jp/english/optical/nano-measurement-technology/ (last access September, 2022).
[38] Yashchuk, V. V., Artemiev, N. A., Lacey, I., McKinney, W. R., and Padmore, H. A., "A new X-ray optics laboratory (XROL) at the ALS: Mission, arrangement, metrology capabilities, performance, and future plans," Proc. SPIE 9206, 92060I/1-19 (2014); doi:10.1117/12.2062042.
[39] Yashchuk, V. V., Artemiev, N. A., Lacey, I., McKinney, W. R., and Padmore, H. A., "Advanced environmental control as a key component in the development of ultra-high accuracy ex situ metrology for x-ray optics," Opt. Eng. 54(10), 104104 (2015); doi: 10.1117/1.OE.54.10.104104.

[40] M. Kanaoka, C. Liu, K. Nomura, M. Ando, H. Takino, Y. Fukuda, H. Mimura, K. Yamauchi, Y. Mori, "Figuring and smoothing capabilities of elastic emission machining for low-thermal-expansion glass optics," J. Vac. Sci. Technol. B2. 2110–213 (2007); https://doi.org/10.1116/1.2789440.
[41] K. Kilaru, D. A. Gregory, B. D. Ramsey, M. V. Gubarev, "Differential deposition technique for figure corrections in grazing-incidence X-ray optic," Opt. Eng. 50, 106501/1-7 (2011); doi: 10.1117/1.3631851.
[42] D. L. Windt, R. Conley, Jr, "Two-dimensional differential deposition: figure correction of thin-shell mirror substrates for X-ray astronomy," SPIE Proc. 9603, 96031H/1-12 (2015); https://doi.org/10.1117/12.2188135.
[43] S. Yokomae, H. Motoyama, H. Mimura, "Development of figure correction system for inner surface of ellipsoidal mirrors," Precis. Eng. 53, 248–251 (2018); https://doi.org/10.1016/j.precisioneng.2018.04.010.
[44] C. Morawe, S. Labouré, J.-C. Peffen, F. Perrin, A. Vivo, R. Barrett, "X-ray mirror figure correction by differential deposition and off-line metrology," J. Synchrotron Rad. 26, 1872–1878 (2019); https://doi.org/10.1107/S1600577519012256.
[45] M. Yabashi, K. Tono, H. Mimura, S. Matsuyama, K. Yamauchi, T. Tanaka, H. Tanaka, K. Tamasaku, H. Ohashi, G. S., T. Ishikawa, "Optics for coherent X-ray applications," J. Synchrotron Rad. 21, 976–985 (2014); doi: 10.1107/S1600577514016415.
[46] V. V. Yashchuk, Optimal Measurement Strategies for Effective Suppression of Drift Errors, Rev. Sci. Instrum. 80, 115101/1-10 (2009); http://dx.doi.org/10.1063/1.3249559.
[47] V. V. Yashchuk, G. Centers, G. S. Gevorkyan, I. Lacey, and B. V. Smith, "Correlation methods in optical metrology with state-of-the-art x-ray mirrors," Proc. SPIE 10612, Thirteenth International Conference on Correlation Optics, 106120O/1-23 (2018); doi: 10.1117/12.2305441.
[48] Takacs, P. Z., Rochester, S., Lacey, I., Munechika, K., and Yashchuk, V. V., "Calibration, modeling, parameterization, and verification of the Instrument Transfer Function of an interferometric microscope," SPIE Optics and Photonics 2022, Conference OP323: Interferometry XXI, Paper No.: 12223-8 (San Diego, August 21-25, 2022); this conference.
[49] Yashchuk, V. V., Munechika, K., Rochester S., Chao, W., Lacey, I., Pina-Hernandez, C., and Takacs, P. Z., "Reliability investigation of the instrument transfer function calibration technique based on binary pseudo-random array standards", in SPIE Optics and Photonics 2022, Conference OP220: Advances in Metrology for X-Ray and EUV Optics X, Paper No.: 12240-25 (San Diego, August 21-25, 2022); this conference.
[50] Griesmann, U., Munechika, K., Renegara, T. B., Zheng, X. A., Soons, J. A., Chao, W., Lacey, I., Pina-Hernandez, C., Takacs, P. Z., and Yashchuk, V. V., "Characterization of surface texture-measuring optical microscopes using a binary pseudo-random array standard," SPIE Optics and Photonics 2022, Conference OP323: Interferometry XXI, Paper No.: 12223-6 (San Diego, August 21-25, 2022); this conference.
[51] Mahajan, V., N., [Optical Imaging and Aberrations. Part I: Ray Geometrical Optics], SPIE, Washington, 1998; Chapter 4.
[52] ISO, 25178-600: Geometrical Product Specification (GPS) – Surface Texture: Areal – Part 600: Metrological Characteristics for Areal-topography Measuring Methods (International Organization for Standardization, 2019); https://www.iso.org/standard/67651.html.
[53] Yashchuk, V. V., Lacey, I., Arnold, T., Paetzelt, H., Rochester, S., Siewert, F., and Takacs, P.Z., "Investigation on lateral resolution of surface slope profilers," Proc. SPIE 11109, 111090M/1-19 (2019); doi: 10.1117/12.2539527.
[54] Stover, J. C., [Optical Scattering: Measurement and Analysis], SPIE, Bellingham, 1995.
[55] ISO, [ISO 15529:2010 − Optics and photonics − Optical transfer function − Principles of measurement of modulation transfer function (MTF) of sampled imaging systems, 3rd edition] ISO/TC 172/SC 1, Geneva, (2010).
[56] de Villiers, G. and Pike, E. R., [The Limits of Resolution], CRC Press, London & New York (2019).
[57] Foreman, M. R., Giusca, C. L., Coupland, J. M., Torok, P., Leach, R. K., "Determination of the transfer function for optical surface topography measuring instruments - a review," Meas. Sci. Technol. 24, 052001/1-18 (2013); doi:10.1088/0957-0233/24/5/052001.
[58] de Groot, P. J., "The instrument transfer function for optical measurements of surface topography," J. Phys. Photonics 3, 024004/1-16 (2021); doi: https://doi.org/10.1088/2515-7647/abe3da.
[59] Barakat, R., "Determination of the Optical Transfer Function Directly from the Edge Spread Function," J. Opt. Soc. Am. 55, 1217-1221 (1965); doi: https://doi.org/10.1364/JOSA.55.001217.
[60] Tatian, B., "Method for Obtaining the Transfer Function from the Edge Response Function," J. Opt. Soc. Am. 55, 1014-1019 (1965); doi: https://doi.org/10.1364/JOSA.55.001014.

[61] Creath, K., "Calibration of numerical aperture effects in interferometric microscope objectives," Appl. Opt. 28 (15), 3333-3338 (1989); doi: 10.1364/AO.28.003333.
[62] Takacs, P. Z., Li, M. X., Furenlid, K., and Church, E. L., "Step-height standard for surface-profiler calibration," Proc. SPIE 1995, 235–244. (1993); https://doi.org/10.1117/12.162661.
[63] Harasaki, A. and Wyant, J. C., "Fringe modulation skewing effect in white-light vertical scanning interferometry," Appl. Opt. 39, 2101-2106 (2000); https://doi.org/10.1364/AO.39.002101.
[64] Boreman, G. D. and Yang, S., "Modulation Transfer Function Measurement Using Three- and Four-bar Targets," Appl. Opt. 34, 8050-8052 (1995); doi: 10.1364/AO.34.008050.
[65] Marchywka, M. and Socker, D. G., "Modulation transfer function measurement technique for small-pixel detectors," Appl. Opt. 31(34), 7198-7213 (1992); doi: ttps://doi.org/10.1364/AO.31.007198.
[66] Nijhawan, O. P., Datta, P. K., and Bhushan, J., "On the measurement of MTF using periodic patterns of rectangular and triangular wave-forms," Nouv. Rev. Opt. 6(1), 33-36 (1975); https://iopscience.iop.org/article/10.1088/0335-7368/6/1/304.
[67] Rhee, H. G., Vorburger, T. V., Lee, J.W., and Fu, J., "Discrepancies between roughness measurements obtained with phase-shifting and white-light interferometry," Appl. Opt. 44(28), 5919-5927 (2005); https://doi.org/10.1364/AO.44.005919.
[68] J. Chu, Q. Wang, J. P. Lehan, G. Gao, and U. Griesmann, "Measuring the phase transfer function of a phase-shifting interferometer," Proc. SPIE 7064, 70640C (2008); https://doi.org/10.1117/12.795243.
[69] J. Chu, Q. Wang, J. P. Lehan, G. Gao, and U. Griesmann, "Spatially resolved height response of phase-shifting interferometers measured using a patterned mirror with varying spatial frequency," Opt. Eng. 49(9), 095601 (2010); doi: 10.1117/1.3488052.
[70] E. Levy, D. Peles, M. Opher-Lipson, and S. G. Lipson, "Modulation transfer function of a lens measured with a random target method," Appl. Opt. 38(4), 679–683 (1999); doi:10.1364/AO.38.000679.
[71] C. R. Wolfe, J. D. Downie, and J. K. Lawson, "Measuring the spatial frequency transfer function of phase-measuring interferometers for laser optics," Proc. SPIE 2870, 553–557 (1996); https://doi.org/10.1117/12.259943.
[72] Barsic, G., Mahovic, S., and Zorc, H., "Development of nano-roughness calibration standards," Meas. Sci. Technol. 23, 035009 (2012); doi:10.1088/0957-0233/23/3/035009.
[73] J. F. Song and T. Vorbuerger, "Standard reference specimens in quality control of engineering surfaces," J. Res. Nation Inst. Stand. Technol. 96, 271–289 (1991); doi:10.6028/jres.096.015.
[74] de Groot, P. J., "Interference Microscopy for Surface Structure Analysis," in T. Yoshizawa, Editor, [Handbook of Optical Metrology: Principles and Applications], 2nd Ed., CRC Press, 2015; Ch. 31, pp. 791-828.
[75] Giusca, C. L. and Leach, R. K., [Measurement Good Practice Guide No. 127: Calibration of the metrological characteristics of coherence scanning interferometers (CSI) and phase shifting interferometers (PSI)], National Physical Laboratory, Teddington, Middlesex, United Kingdom, 2013; ISSN 1368-6550.
[76] Barber, S. K., Anderson, E. D., Cambie, R., McKinney, W. R., Takacs, P. Z., Stover, J. C., Voronov, D. L., and Yashchuk, V. V., "Binary pseudo-random gratings and arrays for calibration of modulation transfer function of surface profilometers," Nucl. Instr. and Meth. A 616, 172-182 (2010); https://doi.org/10.1016/j.nima.2009.11.046.
[77] Yashchuk, V. V., Conley, R., Anderson, E. H., Barber, S. K., Bouet, N., McKinney, W. R., Takacs, P. Z., and Voronov, D. L., "Characterization of electron microscopes with binary pseudo-random multilayer test samples," Nucl. Instr. and Meth. A 649(1), 150-152 (2011); doi: 10.1016/j.nima.2010.11.124.
[78] Yashchuk, V. V., Anderson, E. H., Barber, S. K., Bouet, N., Cambie, R., Conley, R., McKinney, W. R., Takacs, P. Z., Voronov, D. L., "Calibration of the modulation transfer function of surface profilometers with binary pseudo-random test standards: expanding the application range to Fizeau interferometers and electron microscopes," Opt. Eng. 50(9), 093604 (2011); doi: 10.1117/1.3622485.
[79] Yashchuk, V. V., Fischer, P. J., Chan, E. R., Conley, R., McKinney, W. R., Artemiev, N. A., Bouet, N., Cabrini, S., Calafiore, G., Lacey, I., Peroz, C., and Babin, S., "Binary pseudo-random patterned structures for modulation transfer function calibration and resolution characterization of a full-field transmission soft x-ray microscope," Rev. Sci. Instrum. 86(12), 123702/1-12 (2015); doi: 10.1063/1.4936752.
[80] Babin, S., Bouet, N., Cabrini, S., Calafiore, G., Conley, R., Gevorkyan, G., Munechika, K., Vladár, A., and Yashchuk, V. V., "1.5 nm fabrication of test patterns for characterization of metrological systems," Proc. SPIE 10145, 1014518/1-9 (2017); doi:10.1117/12.2257624.

[81] Shapiro, D. A., Babin, S., Celestre, R., Chao, W., Conley, R. P., Denes, P., Enders, B., James, S., Joseph, J., Krishnan, H., Marchesini, S., Nowrouzi, K., Padmore, H., Warwick, T., Yang, L., Yashchuk, V. V., Yu, Y.-S., and Zhao, J., "A facility for ultra-high resolution soft x-ray microscopy and quantitative analysis of chemically heterogeneous nano-materials," Science Advances 6, eabc4904/1-8 (16 December 2020); doi: 10.1126/sciadv.abc4904.

[82] Yashchuk, V. V., Babin, S., Cabrini, S., Griesmann, U., Lacey, I., Munechika, K., Pina-Hernandez, C., and Wang, Q., "Characterization and operation optimization of large field-of-view optical interferometers using binary pseudorandom array test standard," Proc. SPIE 10749, 107490R/1-13 (2018); doi: 10.1117/12.2322011.

[83] Yashchuk, V. V., Babin, S., Cabrini, S., Chao, W., Griesmann, U., Lacey, I., Marchesini, S., Munechika, K., Pina-Hernandez, C., and Roginsky, A., "Binary pseudo-random array test standard optimized for characterization of large field-of-view optical interferometers," Proc. SPIE 11490, 114900W/1-8 (2020); doi: 10.1117/12.2568309.

[84] Lacey, I., Anderson, K., Barnard, H., English, D., McKinney, W. R., Saeed, M. A., and Yashchuk, V. V., "The ALS interferometric microscope upgraded for measurements with large x-ray optics and optical assemblies ", in SPIE Optics and Photonics 2022, Conference OP220: Advances in Metrology for X-Ray and EUV Optics X, Paper No.: 12240-23 (San Diego, August 21-25, 2022); this conference.

[85] T. Etzon, "Construction for perfect maps and pseudorandom arrays," IEEE Trans. on Information Theory 34(5),1308-1316 (1988); doi:10.1109/18.21260.

[86] D. D. Koleske, and S. J. Sibener, "Generation of pseudorandom sequence for use in cross-correlation modulation," Rev. Sci. Instrum. 63(8), 3852-3855 (1992); doi:10.1063/1.1143282.

[87] H. D. Luke and A. Busboom, "Binary arrays with perfect odd-periodic autocorrelation," Appl. Opt. 36(26), 6612-6619 (1999); https://doi.org/10.1364/AO.36.006612.

[88] Fenimore, E. E., and Cannon, T. M., "Coded aperture imaging with uniformly redundant arrays," Appl. Opt. 17(3), 337–347 (1978); doi: ttps://doi.org/10.1364/AO.17.000337.

[89] Caroli, E., Stephen, J. B., Cocco, G. Di., Natalucci, L., and Spizzichino, A., "Coded aperture imaging in x- and gamma-ray astronomy," Space Sci. Rev. 45, 349–403 (1987); doi: https://doi.org/10.1007/BF00171998.

[90] Yan, H., Conley, R., Bouet, N., and Chu, Y. S., "Hard x-ray nanofocusing by multilayer Laue lenses," J. Phys. D: Appl. Phys. 47, 263001 (2014); doi:10.1088/0022-3727/47/26/263001.

[91] R. Conley, B. Shi, M. Erdmann, S. Izzo, L. Assoufid, K. Goetze, T. Mooney, and K. Lauer "APS deposition facility upgrades and future plans", Proc. SPIE 9207, 92070I (2014); https://doi.org/10.1117/12.2062427.

[92] Bradski, G.R and Kaeller, A., [Learning OpenCV- Computer Vision with the OpenCV], 1st Ed., O'Reily Media, Inc., Sebastopol (2008).

[93] Duda, A. and Frese, U., "Accurate Detection and Localization of Checkerboard Corners for Calibration," in: [29th British Machine Vision Conference (BMVC-29)], BMVA Press, Newcastle, 2018; http://bmvc2018.org/contents/papers/0508.pdf.

[94] Hartley, R. and Zisserman, A., [Multiple View Geometry in Computer Vision], Cambridge University Press, New York, 2003.